Received ; | Revised ; | Accepted

DOI: xxx/xxxx

ARTICLE TYPE

A adaptive parameter selection strategy based on maximizing the probability of data for robust fluorescence molecular tomography reconstruction

Jintao Li[1,2] | Lizhi Zhang[1,2] | Diya Zhang[1,2] | Dizhen Kang[1,2] | Beilei Wang[1,2] | Xiaowei He[1,2] | Heng Zhang[1,2] | Yizhe Zhao[1,2] | Hongbo Guo*[1,2] | Yuqing Hou*[1,2]

[1]The Xi'an Key Laboratory of Radiomics and Intelligent Perception, Xi'an, China.
[2]School of Information Sciences and Technology, Northwest University, Xi'an, 710127, China.

Correspondence
*Hongbo Guo, School of Information Sciences and Technology, Northwest University, Xi'an, 710127, China. Email: guohb@nwu.edu.cn. *Yuqing Hou, School of Information Sciences and Technology, Northwest University, Xi'an, 710127, China. Email: houyuqin@nwu.edu.cn

To alleviate the ill-posed of the inverse problem in Fluorescent molecular tomography (FMT), many regularization methods based on L_2 or L_1 norm have been proposed. Whereas, the quality of regularization parameters affect the performance of the reconstruction algorithm. Some classical parameter selection strategies usually need initialization of parameter range and high computing costs, which is not universal in the practical application of FMT. In this paper, an universally applicable adaptive parameter selection method based on maximizing the probability of data (MPD) strategy was proposed. This strategy used maximum a posteriori (MAP) estimation and maximum likelihood (ML) estimation to establish a regularization parameters model. The stable optimal regularization parameters can be determined by multiple iterative estimates. Numerical simulations and *in vivo* experiments show that MPD strategy can obtain stable regularization parameters for both regularization algorithms based on L_2 or L_1 norm and achieve good reconstruction performance.

KEYWORDS:
Fluorescent molecular tomography, Parameter selection, Bayesian approach, morphology recovery, spatial localization

1 | INTRODUCTION

As a non-invasive, no radiation, low cost, high specificity, and sensitivity optical molecular imaging technique, Fluorescence molecular tomography (FMT) can reconstruct the three-dimensional spatial and concentration distribution of fluorescent probes *in vivo*[1,2]. So far, FMT has been widely applied in *in vivo* 3D visualization of liver cancer, glioma, and nasopharyngeal carcinoma[3–5], analysis of pathological tumor characteristics, and evaluation of curative effect of anticancer drug discovery, etc[6–8]. However, due to the high scattering effect of fluorescence in biological tissues, and insufficient optical information detected by CCD camera, FMT reconstruction is highly ill-posed and difficult to obtain accurate solutions[9–11].

To solve the ill-conditioned problem, efficient reconstruction algorithms have been proposed to obtain accurate reconstruction results in FMT. These reconstruction algorithms can be classified into L_2 norm, L_1 norm and $L_p(0 < p < 1)$ norm from the regularization type. With the introduction of Tikhonov regularization, the penalized optimization problem of L_2 norm can be converted into a simple standard quadratic form[12–14], which can be solved by Gauss Newton (GN)[13,15] algorithm and Conjugate Gradient[16] algorithm. These algorithms have realized effective computation and stable solution of the inverse problem to varying degrees. However, the L_2-regularization approaches often produce too smooth

reconstruction results for early tumor detection. Based on the Compressed Sensing (CS) theory[17], the reconstruction signals are considered to be sufficiently sparse. Thus, plenty of L_1 norm reconstruction algorithms have been proposed in FMT research, including adaptive support driven reweighted L_1-regularization (ASDR-L1)[18] algorithm, sparsity adaptive subspace pursuit (SASP)[19] algorithm and incomplete variables truncated conjugate gradient(IVTCG)[20] algorithm. And a large number of experiments have proved that these L_1 algorithm can overcomes the over-smoothing problem of L_2 algorithm and improve the spatial resolution and location accuracy. In recent years, some non-convex $L_p(0 < p < 1)$ regularization algorithms have been proposed to further enhance the sparsity of the solution[21], including non-convex sparse regularization approach (nCSRA) framework[22], half thresholding pursuit algorithm (HTPA)[23] and efficient matrix-free method[21]. These algorithms further improved the computational memory, spatial resolution and reconstruction accuracy. All in all, these above proposed reconstruction algorithms for L_2, L_1 and L_p norm can achieve excellent reconstruction results. However, for different application scenarios of FMT reconstruction, the quality of regularization parameters will directly affect the results of the reconstruction algorithm. Some research results show that large regularization parameter will deviate the reconstructed solution from the true distribution, while small regularization parameter will contribute little to the regularization of the problem. Therefore, how to determine the regularization parameters effectively is very important in the practical application process of FMT.

After a lot of investigation, the existing regularization parameter selection methods can be divided into three categories. Firstly, for L_2 norm regularization, commonly used parameter choices include L-curve and U-curve. The essence of the L-curve is to draw a comparison plot between the solution norm and the residual norm to find the point with the maximum curvature value[24]. Based on the L-curve, the U-curve is the reciprocal curve of the regularization norm and the corresponding residual norm[25,26]. The L-curve and U-curve have been verified extensively in the field of gravitational[27], electrochemistry[28] and DFMT[29], which can guarantee the reconstruction algorithms to obtain higher imaging resolution and accuracy. Secondly, the L_1-curve was used to select a good regularization parameter for L_1 norm regularization by defining the best trade-off between the L_2 norm of the residual and the L_1 norm of the solution. Theoretically, the value selected on the L_1-curve reduces the number of iterations required for reconstruction and the time cost required for reconstruction. Therefore, L_1-curve can be used in the large-scale L_1 norm regularization problem. Many studies show that L_1-curve can significantly improve the reconstruction accuracy and robustness[30,31] in fields such as Electrical impedance tomography (EIT) and X-ray fluorescence computed tomography (XFCT). Thirdly, there are also some general parameter selection methods that are suitable for both L_1 and L_2 norm solutions, such as generalized cross-validation (GCV)[32]. The GCV method takes the minimum sum of squares of residual terms as the optimal regularization parameter from the perspective of statistics by exploiting prior information on the observed signal without other additional information[33]. Busby et al. numerically investigated the application of GCV and L-curve methods to regularization parameter selection for finite element inverse dynamics problems[34]. The results show that GCV and L-curve are indeed good methods for selecting optimal smoothing parameters. Based on Bayesian theory, by directly introducing the iteration parameters based on L_2 into the iteration based on L_1, Sanders et al. proposed an iteration scheme for selecting regularization parameters in the inverse problem of image processing, which obtained accurate convergence results[35]. In summary, for most cases with white noise or even filtered white noise, the regularization parameter selection strategies proposed above can achieve satisfactory results. However, these methods need to specify a reasonable range of parameter values before selecting the regularization parameters. If the parameter range is not appropriate, the computational cost may increase and the desired result may not be achieved. And for L-curve, U-curve and L_1-curve, they are only suitable for specific application scenarios and are not universally applicable. Moreover, for highly ill-posed conditions, these curves above may not be able to obtain obvious inflection points. At the same time, compared with L-curve, U-curve and L_1-curve, the calculation cost of GCV is higher due to multiple solution calculation, especially for large systems matrix. In addition, based on Bayesian theory, there are some differences between L_2 and L_1 regularization in the reconstruction of FMT. And the regularization parameter selection strategy needs to be further improved to be applicable in the field of FMT. Therefore, how to construct a universally applicable and high-efficiency regularization parameter selection strategy is the focus of this paper.

In Bayesian statistics research, some important prior information can be obtained by using maximum a posteriori probability estimation. Inspired by it, for most widely used L_1-norm and L_2-norm based regularization algorithms, we proposed an adaptive parameter selection strategy based on maximizing the probability of data (MPD) in FMT research. Taking advantages of the maximum a posteriori (MAP) estimation and maximum likelihood (ML) estimation, MPD strategy is an iterative estimation scheme to build the relationship between the variance and regularization parameters. After a series experiments, MPD strategy was demonstrated to converge accurately and helpful to achieve high-precision FMT reconstructions. The

structure of this paper is organized as follows: Section 2 introduces the MPD strategy. Section 3 and 4 elaborates the details of the simulation experiments and the *in vivo* data source and presents the experimental results. Section 5 discusses the performance of MPD and makes a conclusion.

2 | MATERIALS AND METHODS

2.1 | Photon propagation model

For steady-state FMT with point excitation sources, the diffusion equations (DE) have been commonly used to model the forward problem of FMT. In the finite element framework, considering the error of FMT during data acquisition and processing, we can obtain the following linear model[36,37]:

$$\mathrm{Ax} = \mathrm{b} + \xi \tag{1}$$

where A is the system matrix; x and b represent the distribution of the unknown fluorescent source and the measurements of surface photon distribution, respectively.

In the actual process, the constructed optical transmission equation and the estimated optical parameters lead to some errors in the mathematical model. Secondly, there is some noise in the signal collected by the camera. Therefore, the error vector $\xi \in \mathrm{R}^{m\times 1}$ refers to two aspects of error: model error caused by the system matrix A and additive noise caused by the b.

2.2 | The selection strategy of regularization parameter value based on MPD

For FMT reconstruction under Bayesian theory, it is the maximum a posteriori (MAP) estimate of distribution of the unknown fluorescence source x, when given the known measurement vector b. Therefore, Eq. (1) can be transformed into the follow equation[38]:

$$\mathrm{x}_{\mathrm{MAP}} = \arg\max_{\mathrm{x}} \mathrm{p}(\mathrm{x} \mid \mathrm{b}) = \arg\max_{\mathrm{x}} \mathrm{p}(\mathrm{b} \mid \mathrm{x})\mathrm{p}(\mathrm{x}) \tag{2}$$

Take the negative logarithm on both sides of Eq. (2) to obtain the following equation:

$$\begin{aligned} \mathrm{x}_{\mathrm{MAP}} &= \arg\min_{\mathrm{x}} -\log \mathrm{p}(\mathrm{x} \mid \mathrm{b}) \\ &= \arg\min_{\mathrm{x}} -\log \mathrm{p}(\mathrm{b} \mid \mathrm{x}) - \log \mathrm{p}(\mathrm{x}) \end{aligned} \tag{3}$$

where p(x | b) represents the posterior probability of the unknown fluorescence source x given the measured b. p(b | x) and p(x) is the likelihood probability (measurement model) and the prior probability (prior model), respectively.

In the process of FMT data acquisition, we consider that the mutually independent measurement noise follow normal distribution i.e. $\xi \sim \mathrm{N}\left(0, \sigma^2\right)$[39]. Thus, p(ξ) is defined as:

$$\mathrm{p}(\xi) = (2\pi\sigma)^{-m/2} \exp\left(-\frac{\xi^2}{2\sigma^2}\right) \tag{4}$$

Furthermore, based on Eq. (1), we can further get p(b | x) with $\mathrm{p}(\xi) = \mathrm{N}(0, \sigma^2)$:

$$\begin{aligned} \mathrm{p}(\mathrm{b} \mid \mathrm{x}) &= \mathrm{p}(\mathrm{b} \mid \mathrm{x}, \sigma) \\ &= (2\pi\sigma)^{-m/2} \exp\left(-\frac{\|\mathrm{Ax} - \mathrm{b}\|_2^2}{2\sigma^2}\right) \end{aligned} \tag{5}$$

Substitute Eq. (5) into (3) to get:

$$\mathrm{x}_{\mathrm{MAP}} = \arg\min_{\mathrm{x}} \frac{\|\mathrm{Ax} - \mathrm{b}\|_2^2}{2\sigma^2} - \log \mathrm{p}(\mathrm{x}) \tag{6}$$

where the likelihood function partially corresponds to the loss function, and the prior probability partially corresponds to the regular term.

For L_2 regularization: The x belongs to the Gaussian distribution, i.e. $\mathrm{x} \sim \mathrm{N}\left(0, \eta^2\right)$, in which η^2 is the variance of the signal. Thus, p(x) can be defined as:

$$\mathrm{p}(\mathrm{x}) = \mathrm{p}(\mathrm{x} \mid \eta) = \frac{\det \mathrm{T}}{\left(2\pi\eta^2\right)^{\mathrm{n}/2}} \exp\left(-\frac{\|\mathrm{Tx}\|_2^2}{2\eta^2}\right) \tag{7}$$

where $\mathrm{T} \in \mathrm{R}^{n\times n}$ represents the unit matrix. And Eq. (6) can be transformed into the follow equation:

$$\begin{aligned} \mathrm{x}_{\mathrm{MAP}} &= \arg\min_{\mathrm{x}} \frac{\|\mathrm{Ax} - \mathrm{b}\|_2^2}{2\sigma^2} + \frac{\|\mathrm{Tx}\|_2^2}{2\eta^2} \\ &= \arg\min_{\mathrm{x}} \left(\|\mathrm{Ax} - \mathrm{b}\|_2^2 + \frac{\sigma^2}{\eta^2}\|\mathrm{Tx}\|_2^2\right) \\ &= \arg\min_{\mathrm{x}} \|\mathrm{Ax} - \mathrm{b}\|_2^2 + \lambda\|\mathrm{Tx}\|_2^2 \end{aligned} \tag{8}$$

Hence, we get the expression of the regularization parameter: $\lambda = \sigma^2/\eta^2$.

For L_1 regularization: The solution x follows a Laplace distribution, with the mean and the variance of zero and ζ^2, respectively. Thus, p(x) can be defined as:

$$\mathrm{p}(\mathrm{x}) = \mathrm{p}(x \mid \zeta) = \frac{\det \mathrm{T}}{(\sqrt{2}\zeta)^n} \exp\left(-\frac{\|\mathrm{Tx}\|_1^1}{\zeta/\sqrt{2}}\right) \tag{9}$$

Then Eq. (6) can be transformed into the follow equation:

$$\begin{aligned} \mathrm{x}_{\mathrm{MAP}} &= \arg\min_{\mathrm{x}} \left(\|\mathrm{Ax} - \mathrm{b}\|_2^2 + \frac{2\sigma^2}{\zeta/\sqrt{2}}\|\mathrm{Tx}\|_1^1\right) \\ &= \arg\min_{\mathrm{x}} \|\mathrm{Ax} - \mathrm{b}\|_2^2 + \lambda\|\mathrm{Tx}\|_1^1 \end{aligned} \tag{10}$$

So, we can obtain an expression for the regularization parameter of L_1 norm: $\lambda = 2^{3/2}\sigma^2/\zeta$.

Therefore, in this paper, we use the iteration idea to find a good estimates of σ, η and ζ to determine λ. First, we took the initial λ_0 as prior information to solve x by using the given regularization algorithm. Then, the solved x was taked as a given condition to calculate the variance of the distributions

of (Ax-b) and (Tx), respectively. Based on two previous representation, we obtained the updated value of λ. And so on, we got a stable λ value through repeated iterations. The specific methods are as follows:

1.Calculate x_λ when given value of λ_0:

In this paper, we adopt the L_2-norm_Tikhonov regularization reconstruction algorithm[14] and the L_1-norm_IVTCG regularization reconstruction algorithm[20] to solve x_λ according to given λ_0, respectively.

2.Determin σ and η based on the caculated x_λ: In Eq. (5), σ is the variance of the (Ax-b) distribution. In Eq. (7) and (9), η and ζ are the variances of (Tx) belonging to Gaussian and Laplace distributions, respectively. Therefore, based on the x_λ obtained in the first step, we can find the expressions about σ, η and ζ by the law of total probability under the idea of maximum likelihood (ML) estimation.

For L_2 norm: The p(x) belongs to the Gaussian distribution, using the law of total probability leads to:

$$\begin{aligned} p(b) &= \int p(b \mid x)p(x)dx \quad x \in R^n \\ &= \left(2\pi\sigma^2\right)^{-m/2}\left(2\pi\eta^2\right)^{-n/2}\det \\ &\int \exp\left(-\frac{\|Ax-b\|_2^2}{2\sigma^2}-\frac{\|Tx\|_2^2}{2\eta^2}\right)dx \end{aligned} \tag{11}$$

Differentiating Eq. (11) with respect to σ and setting the derivatives to zero, we can get an iterative expression about σ:

$$\begin{cases} \frac{d}{d\sigma}p(b) = -\frac{m}{\sigma}p(b) + \sigma^{-3}p(b)E\left[\|Ax-b\|_2^2 \mid b\right] & (12) \\ \sigma_{i+1}^2 = \frac{1}{m}E\left[\|Ax_{\lambda_i}-b\|_2^2 \mid b\right] & (13) \end{cases}$$

where i is the number of iterations from zero, x_{λ_i} is a regularized solution with a regularization parameter of λ_i at the ith iteration.

Differentiating Eq. (11) with respect to η and setting the derivatives to zero leads to:

$$\eta_{i+1}^2 = \frac{1}{n}E\left[\|Tx_{\lambda_i}\|_2^2 \mid b\right] \tag{14}$$

where the expansion of conditional expectation can be described by Lemma 7.2 of[40] and Lemma 1 of[35] as follow:

$$\begin{cases} E[f(x) \mid b] = E\left[f\left(x_\lambda + \sigma H^{-1/2}U\right)\right] & (15) \\ E\left(\|f + B\xi\|_{\mathcal{H}}^2\right) = \|f\|_{\mathcal{H}}^2 + \sigma^2\,\mathrm{trace}\left(B^*B\right) & (16) \end{cases}$$

where f(x) is an arbitrary function, x_λ is the solution of the functional equation, $H = A^TA + \lambda T^TT$, $U \sim N(0, I)$, $f \in \mathcal{H}$, $\mathcal{H}$ is a deterministic, real Hilbert space, ξ be a discrete noise vector, $B : R^n \to \mathcal{H}$ be a (bounded) linear operator.

Let $f(x) = \|Ax_{\lambda_i} - b\|_2^2$, then expanding Eq. (13) and applying Eq. (15) and (16) leads to:

$$\begin{aligned} m\sigma_{i+1}^2 &= E\left[\|Ax_{\lambda_i}-b\|_2^2 \mid b\right] \\ &= E\left[\left\|A\left(x_{\lambda_i}+\sigma_{i+1}H^{-1/2}U\right)-b\right\|_2^2\right] \\ &= \left\|Ax_{\lambda_i}-b\right\|_2^2 + \sigma_{i+1}^2\,\mathrm{trace}\left(H_i^{-1}\,A^TA\right) \end{aligned} \tag{17}$$

where $H_i = A^TA + \lambda_i T^TT$. Similarly, let $f(x) = \|Tx_{\lambda_i}\|_2^2$, expanding Eq. (14) leads to:

$$\begin{aligned} n\eta_{i+1}^2 &= E\left[\|Tx_{\lambda_i}\|_2^2 \mid b\right] \\ &= \left\|Tx_{\lambda_i}\right\|_2^2 + \lambda_i\eta_{i+1}^2\mathrm{trace}\left(H_i^{-1}T^TT\right) \end{aligned} \tag{18}$$

According to Eq. (17) and (18), doing simple mathematical derivation leads to:

$$\begin{cases} \sigma_{i+1}^2 = \left\|Ax_{\lambda_i}-b\right\|_2^2 / \left(m - \mathrm{trace}\left(H_i^{-1}A^TA\right)\right) & (19) \\ \eta_{i+1}^2 = \left\|Tx_{\lambda_i}\right\|_2^2 / \left(n - \lambda_i\,\mathrm{trace}\left(H_i^{-1}T^TT\right)\right) & (20) \end{cases}$$

For L_1 norm: The p(x) belongs to the Laplace distribution, using the law of total probability leads to:

$$\begin{aligned} p(b) &= \left(2\pi\sigma^2\right)^{-m/2}\left(\sqrt{2}\zeta\right)^{-n}\det \\ &\int \exp\left(-\frac{\|Ax-b\|_2^2}{2\sigma^2}-\frac{\|Tx\|_1^1}{\zeta/\sqrt{2}}\right)dx \quad x \in R^n \end{aligned} \tag{21}$$

Differentiating Eq. (21) with respect to σ and setting the derivatives to zero leads to:

$$\sigma_{i+1}^2 = \frac{1}{m}E\left[\|Ax_{\lambda_i}-b\|_2^2 \mid b\right] \tag{22}$$

Meanwhile, differentiating Eq. (21) with respect to ζ and setting the derivatives to zero leads to:

$$\begin{cases} \frac{d}{d\zeta}p(b) = -\frac{n}{\zeta}p(b) + \sqrt{2}\zeta^{-2}p(b)E\left[\|Tx_{\lambda_i}\|_1^1 \mid b\right] & (23) \\ \zeta_{i+1} = \frac{\sqrt{2}}{n}E\left[\|Tx_{\lambda_i}\|_1^1 \mid b\right] & (24) \end{cases}$$

Similarly, let f(x) equals to $\|Ax_{\lambda_i}-b\|_2^2$ and $\|Tx_{\lambda_i}\|_1^1$, respectively. For Eq. (22) and (24), applying Eq. (15) and (16) leads to:

$$\begin{cases} m\sigma_{i+1}^2 = \left\|Ax_{\lambda_i}-b\right\|_2^2 + \sigma_{i+1}^2\,\mathrm{trace}\left(H_i^{-1}\,A^TA\right) & (25) \\ \frac{n}{\sqrt{2}}\zeta_{i+1} = \sqrt{\left\|Tx_{\lambda_i}\right\|_1^2 + \lambda_i\zeta_{i+1}\mathrm{trace}\left(H_i^{-1}T^TT\right)} & (26) \end{cases}$$

The solution of Eq. (25) is shown in Eq. (19), while the solution of Eq. (26) belongs to a quadratic equation of one unknown. From the formula, it can be observed that $\Delta = b^2 - 4ac = \left(2\lambda_i\,\mathrm{trace}\left(H_i^{-1}\,T^TT\right)\right)^2 + 8n^2\left\|Tx_{\lambda_i}\right\|_1^2 > 0$, which proves that ζ has a solution. Therefore, doing simple

mathematical derivation leads to:

$$\zeta_{i+1} = \left(2\lambda_i \,\mathrm{trace}\left(\mathrm{H}_i^{-1}\,\mathrm{T}^{\mathrm{T}}\mathrm{T}\right) + \sqrt{\Delta}\right)/2n^2 \tag{27}$$

3.Update λ according to variance:

For L_2 norm and L_1 norm, we can update the regularization parameters by the formula $\lambda_{i+1} = \sigma_i^2/\eta_i^2$ and $\lambda_{i+1} = 2^{3/2}\sigma_i^2/\zeta_i$, respectively. And it can be seen that it only slightly depends on λ_0 for updating the regularization parameters. Based on the above statements, the pseudocode for the MPD strategy is given in Algorithm 1.

Algorithm1 MPD strategy

Input: system matrix A, Surface photon measurements b, initial regularization parameter λ_0, identity matrix T, rows of the system matrix n, columns of the system matrix m.
Initialize: $\mathrm{a} = \mathrm{A}^{\mathrm{T}}\mathrm{A}$, $\mathrm{t} = \mathrm{T}^{\mathrm{T}}\mathrm{T}$.
For $i = 0$ **to** i **do**
If: The optimization objective function satisfied as
$\mathrm{x}_{\mathrm{MAP}} = \arg\min \|\mathrm{Ax} - \mathrm{b}\|_2^2 + \lambda\|\mathrm{Tx}\|_2^2$
Step1: Use λ_i to calculate x_{λ_i} by the given L_2 norm reconstruction algorithm.
Step2: Determin σ and η based on the caculated x_{λ_i}, Eq.(19) and Eq.(20).
Step3:Update λ according to σ and η: $\lambda_{i+1} = \sigma_i^2/\eta_i^2$
Else if: The optimization objective function satisfied as
$\mathrm{x}_{\mathrm{MAP}} = \arg\min \|\mathrm{Ax} - \mathrm{b}\|_2^2 + \lambda\|\mathrm{Tx}\|_1^1$
Step1: Use λ_i to calculate x_{λ_i} by the given L_1 norm reconstruction algorithm.
Step2: Determin σ and ζ based on the caculated x_{λ_i}, Eq.(19) and Eq.(27).
Step3:Update λ according to σ and ζ: $\lambda_{i+1} = 2^{3/2}\sigma_i^2/\zeta_i$
End for

3 | EXPERIMENTS SETTING

3.1 | Numerical simulation

The trunk of the mouse model was selected for the simulation study, which was divided into six non-homogeneous three-dimensional digital mouse models: muscle, heart, lung, liver, stomach and kidney, as shown in Fig. 1(a). In the simulation experiments, the fluorescence yield was set to $0.5mm^{-1}$, and the excitation and emission wavelength are 650 *nm* and 670 *nm*, respectively. The relevant optical properties of the various organs of the digital mouse are in[41]. To evaluate the performance of the MPD strategy, we designed effectiveness and robustness experiments, respectively.

Effectiveness experiments: Previous studies have shown that the L_2 and L_1 reconstruction algorithm are suitable for solving large and small size fluorescence source,respectively[14]. Therefore, in order to verify the effectiveness of the MPD strategy for L_2 and L_1 regularization algorithm, we designed different sizes of fluorescence source in single source experiments. The specific parameters are as follows: For the L_2 norm, a large sizes light source with a radius of $2mm$ was placed in the liver with a central location of $(15, 8, 15mm)$, as shown in Fig. 1(b). Meanwhile, for the L_1 norm, a small sizes light source with a radius of $1mm$ was placed in the liver with a central location of $(15, 8, 15mm)$, as shown in Fig. 1(c).

Robustness experiments: We further performed a set of dual-source experiments to verify the robustness of the MPD strategy. For the L_2 norm, two light sources of the radius of $2mm$ were placed in the liver, with a central location of $(15, 9, 15mm)(22.5, 9, 15mm)$, as shown in Fig. 1(d). Meanwhile, for the L_1 norm, two light sources of the radius of $1mm$ were placed in the liver, with a central location of $(15, 8, 15mm)(22.5, 8, 15mm)$, as shown in Fig. 1(e).

Throughout the experiment, the diffusion equations(DE) based on the finite element method was used to obtain a specific surface energy distribution, as shown in Fig. 1(g)-(j). In the process of FMT reconstruction, the mouse model was discretized into 10372 nodes and 52892 tetrahedral elements, as shown in Fig. 1(f).

3.2 | In vivo imaging experiment

In *in vivo* experiment, in order to prevent light scattering artifacts caused by fur, two female BALB/C nude mice (4-6 weeks old) was adopted. All experimental procedures were under the approval of the Animal Ethics Committee of the Northwest University of China[41]. And all animal procedures were performed under isoflurane gas anesthesia (3% isoflurane air mixture) to minimize pain to mice. Prior to the FMT reconstruction, some essential preprocessing operations were carried out.

Pseudotumor mouse model: To evaluate the practicability of MPD strategy, two sets of *in vivo* experiments based on different size pseudotumor were conducted. The Cy5.5 solution ($0.01mg/ml$, Excitation wavelength: $671nm$) was added to the transparent glass tube as the pseudotumor. To verify the practicability of the MPD strategy for L_2 regularization algorithm, a transparent glass tube with an inner radius of 1.5mm and a height of 5.5mm was implanted into the region between the liver and the lungs. While verifying the practicability of the MPD strategy for L_1 regularization algorithm, a small size glass tube with an inner radius of 1mm was implanted into the abdominal cavity.

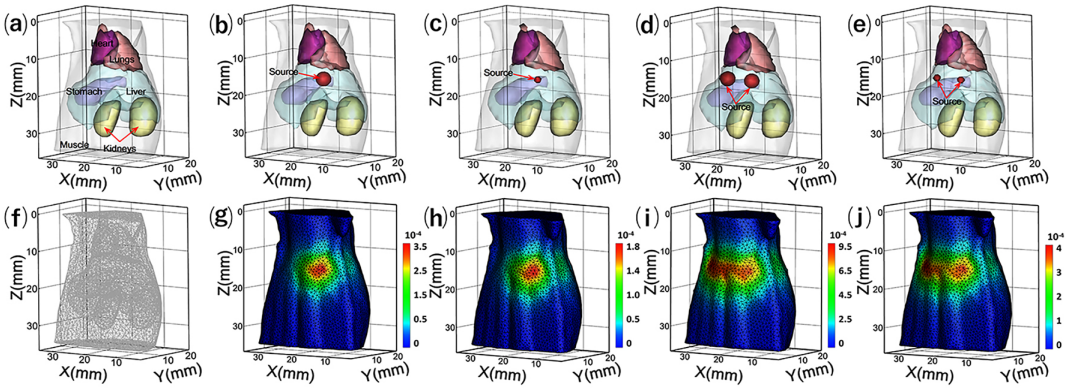

FIGURE 1 Numerical simulation settings. (a) The trunk part of the digital mouse. (b)-(c) Simulated model views of the single-source. (d)-(e) Simulated model views of the dual-source. (f) The uniform tetrahedral mesh for the inverse reconstruction problem. (g)-(j) The simulated distribution of forward mesh and surface photon density when the fluorescence source are (b)-(e).

Data acquisition and processing: In optical acquisition process, the EMCCD camera was cooled to −80°C to reduce the effects of thermal noise. A 670nm continuous wave semiconductor laser is used to reflect the excitation fluorescence probe. A band-pass filter centered on the wavelength of 740nm is placed in front of the highly sensitive TE-cooled backilluminated EMCCD camera to collect fluorescence signals[14,22]. The exposure times for fluorescence and white light were set to 2 seconds and 0.25 seconds, respectively. In the CT volume acquisition process, after some needed preparations (tube warming up, X-ray calibration, and CT attenuation-corrected), the tube voltage and tube power were set as 70kVp and 39W. And the rotating stage was rotating 360 degrees with 1° intervals to capture the X-ray projection images. Then, the projection data were reconstructed by Feldkamp-Davis-Kress (FDK) reconstruction algorithm. For FMT reconstruction, the mouse model was discretized into tetrahedral mesh by amria 5.2 (amria, visage imaging, Australia). All experimental codes were written in MATLAB2020 and executed on a desktop computer with 2.60GHz Intel processor I5-11400Fand 16G RAM.

3.3 | Algorithm comparison and evaluation index

Because our proposed MPD strategy can be applied not only to L_2 regularization algorithms but also to L_1 regularization algorithms. Thus, after preliminary investigation, L-curve[24] and U-curve[25] were used as comparison strategies for determing the regularization parameter of L_2-norm problem. GCV curve[32] and L_1-curve[31] were used as comparison strategies for L_1-norm regularization parameter selection. Since the focus of this paper is to verify the effectiveness of MPD strategy, the traditional algorithms Tikhonov[15] based on L_2-norm and IVTCG base on L_1-norm[20] were chosen as validation algorithm, rather than some more sophisticated algorithms. In addition, the location error (LE) and Dice index[12] were used to evaluate the reconstructed results based on different regularization parameter selection strategies.

4 | EXPERIMENT RESULTS

4.1 | Numerical simulations results

4.1.1 | Effectiveness experiment

MPD strategy for L_2: Fig.2 shows the simulation reconstruction results of Tikhonov algorithm with three regularization parameter selection strategy. Based on the experiential value ranges $\left(1e^{-5}, 1e^{2}\right)$ of L-curve method and U-curve method, the log-log plots of 40 regularization parameters is shown in Fig. 2(a) and (c). It can be observed that the L-curve shows an easily discernible inflection point($\lambda = 3.1256e^{-4}$) in Fig. 2(a), and the minimum point($\lambda = 3.2346e^{-4}$) of the U-curve can be easily detected in Fig. 2(c). For the proposed MPD strategy, Fig. 2(e) represents the change curve of regularized parameter at three different initial values. It can be seen that a relatively stable point($\lambda = 1.4584e^{-4}$) was obtained from the fourth iteration. The corresponding 3D reconstruction results of the three regularization parameters obtained are shown in Fig. 2 (b), (d) and (f), and the quantitative indicators are shown in Table 1.

As can be seen from the 3D view in Fig.2, since the regularization parameters selected by the three strategies are on the same order of magnitude, the corresponding reconstruction results are similar in distribution. Under three determined regularization parameters, the Tikhonov algorithm can accurately reconstruct the position of the source. However, some slight differences can be observed in the transverse view. As shown in Fig. 2 (b) and (d), the reconstruction results of regularization parameters selected by L-curve and U-curve strategies have a

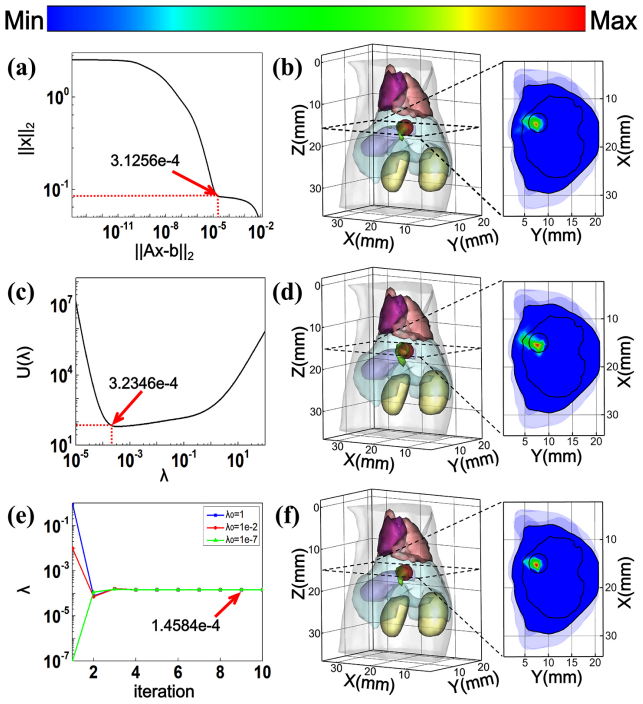

FIGURE 2 Simulation reconstruction results of Tikhonov algorithm with regularization parameter selection strategy. (a), (c) and (e) represent the curve results solved by using L-curve algorithm, U-curve algorithm and MPD algorithm. (b), (d) and (f) respectively represent the reconstruction results of the corresponding regularization parameters.

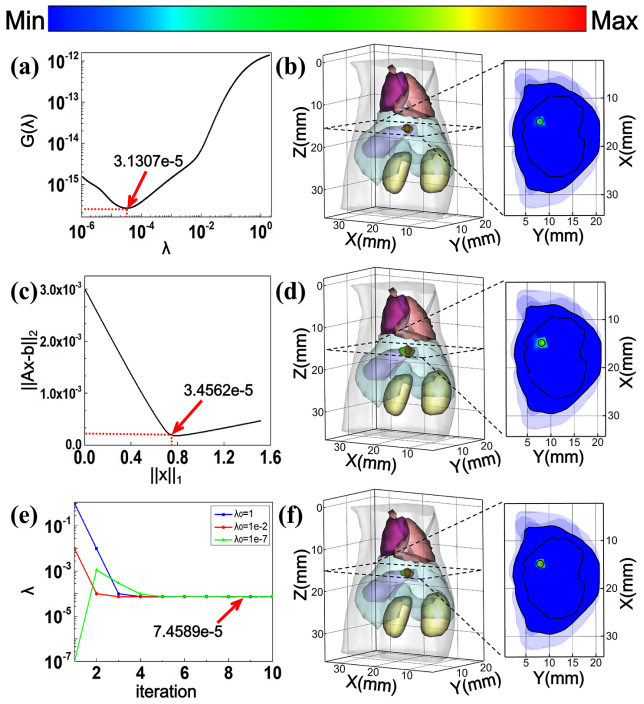

FIGURE 3 Simulation reconstruction results of IVTCG algorithm with regularization parameter selection strategy. (a), (c) and (e) represent the curve results solved by using GCV curve algorithm, L_1-curve algorithm and MPD algorithm. (b), (d) and (f) respectively represent the reconstruction results of the corresponding regularization parameters.

tendency of outward diffusion accompanied by large artifacts. In contrast, the regularization parameters selected by our proposed MPD strategy can well suppress this trend, as shown in Fig.2 (f). The highest Dice in Table1 further indicates the advantage of the MPD strategy in shape recovery.

MPD strategy for L_1: Fig.3 shows the simulation reconstruction results of IVTCG algorithm with regularization parameter selection strategy. By experience, the value range of regularization parameter based on GCV curve and L_1-curve methods are set as $(1e^{-6}, 1)$. Fig. 3(a) and (c) represent the log-log plots of the 40 regularization parameters. It can be observed that the final result of the GCV curve and L_1-curve are $3.1307e^{-5}$ and $3.4562e^{-5}$, respectively. Fig. 3(e) represents the regularization parametric curves obtained by using the MPD method at three different initial values, a relatively stable point($\lambda = 7.4589e^{-5}$) was obtained from the sixth iterations.

It can be seen from the 3D view in Fig.3 that regularization parameters selected by IVTCG based on all of the three strategies can reconstruct the position of the source. However, as shown in Fig. 3(b) and (d), the reconstructed results using GCV and L_1-curve strategies are subtle difference from that of the real source, and there are some artifacts. In contrast, the shape of the reconstruction result under the MPD strategy is closer to the real source with more smaller artifacts, as shown in Fig.3(f). And the transverse view further shows that the reconstruction center is closer to the real source. In conclusion, the reconstruction results of L_1 algorithm under MPD strategy are better than those under GCV and L_1-curve strategy. The index in Table 1 also verifies the effectiveness of our proposed strategy from the side. The reconstruction results of MPD have the smallest LE(0.3426*mm*) and the highest Dice(73%).

4.1.2 | Robustness experiment

Fig.4 shows the results of robustness experiments by using Tikhonov algorithm and the IVTCG algorithm combined with MPD strategy in dual souce reconstruction cases. At three different initial values, the curves of L_2 and L_1 regulazation parameter were displayed in Fig. 4(a) and (c). For L_2-norm paramenter search, although there is a slight fluctuation, all curves tend to be a stable value $\lambda = 1.9482e^{-4}$. For L_1-norm

TABLE 1 Quantitative results of single-source reconstruction experiment.

Group	Method	λ	Reconstruction Center(mm)	LE(mm)	Dice(%)
Tikhonov	L-curve	$3.12e^{-4}$	(15.75, 8.01, 14.86)	0.76	46
	U-curve	$3.23e^{-4}$	(15.76, 8.01, 14.85)	0.77	45
	MPD curve	$1.45e^{-4}$	(14.75, 7.25, 14.93)	0.76	54
IVTCG	GCV curve	$3.13e^{-5}$	(14.88, 7.96, 14.45)	0.56	64
	L_1-curve	$3.45e^{-5}$	(15.23, 7.95, 15.43)	0.49	61
	MPD curve	$7.45e^{-5}$	(14.79, 8.14, 15.24)	0.34	73

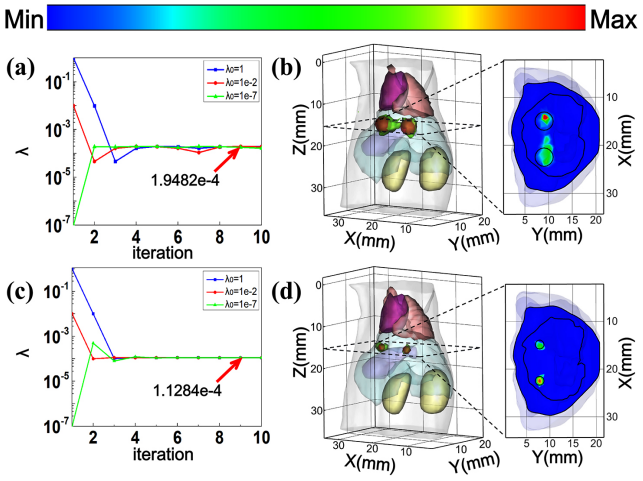

FIGURE 4 Reconstruction results of dual-sources simulation experiments with MPD strategy. (a) and (c) represent the curves in the case of MPD strategy.(b) and (d) represent the reconstruction results of corresponding regularization parameters.

paramenter search, MPD strategy can obtain stable regularization parameters in the sixth iteration, resulting in $\lambda = 1.1284e^{-4}$.

From the 3D view, it can be seen that both L_2 and L_1 algorithms can reconstruct the distribution of real sources based on these determined regularization parameters. As shown in Fig.4(d), the reconstructed source size of IVTCG algorithm is very close to the actual source with Dice of 71%, and the spatial positioning of two sources is accurate with LE less than 0.3mm. For the Tikhonov algorithm, the reconstructed source in a lower position has some artifacts in the transverse view. This phenomenon was also presented in some other studies based on manually selected parameters, which is caused by its oversmoothness of L_2 regulazation algorithm ranther than the improper regularization parameters. Apart from this, by using the MPD strategy, two sources were still distinguished clearly in 3D view with acceptable positional accuracy, as shown in Fig. 4(b). It can be concluded that the regularization parameters determined by the MPD strategy are valid for both L_2 and L_1 algorithms.

4.2 | In vivo imaging experiment

MPD strategy for L_2: Fig.5 shows the *in vivo* reconstruction results of Tikhonov algorithm with regularization parameter selection strategy. Based on the setted parameter range of Tikhonov algorithm $\left(1e^{-7}, 1e^{-2}\right)$, the log-log plots of L-curve and U-curve methods are shown in Fig. 5(a) and (c). It can be seen that the maximum curvature point of the L-curve and the minimum point of the U-curve can be caculated as $\lambda = 1.7146e^{-5}$ and $5.7326e^{-5}$, respectively. After seventh iteration, no matter what the initial value is, the MPD method also converges to a relatively stable solution at $\lambda = 1.6052e^{-5}$, as shown in Fig. 5(e). The corresponding reconstruction results and the quantitative indexs are shown in Fig. 5(b)-(f) and Table 3, respectively. In 3D view, the red area is the actual radiation source, and the green area is the reconstructed radiation source. For better display and envalate the performance, the reconstructed fluorescence image was oberlaied by the CT image incoronal view (C), sagittal view (S) and the transversal view (T), respectively. The black curve represents the actual location of the light source and was marked with the letter S in yellow. Fron CT images, we can confirm that the fluorescence source was located at $(52.45, 54.06, 45.19mm)$. And the source margin was represented by the black dotted curve.

As can be seen from the 3D view in Fig.5, Tikhonov algorithm can accurately reconstruct the distribution of real sources under the three regularization parameter selection strategies. And the reconstructed results are very similar with nearly Dice and LE value, as shown in Table 3. By fusing reconstructed images with CT sections, small differences can be observed from the S, C and T views in Fig.5 (b)-(f). Among them, due to the close regularization parameters selected by MPD and L-curve strategies, the reconstructed source distribution are almost exactly the same, with a small position deviation ($LE = 0.54mm$) from the actual source and greater

TABLE 2 Quantitative results of dual-sources reconstruction experiment.

Group	Center (*mm*)	λ	Reconstruction Center(*mm*)	LE(*mm*)	Dice(%)
Tikhonov	(22.5, 9.0, 15)	$1.94e^{-4}$	(21.12, 10.20, 15.07)	1.80	46
	(15.0, 9.0, 15)		(14.25, 9.56, 15.25)	0.97	
IVTCG	(22.5, 8.0, 15)	$1.12e^{-4}$	(22.65, 7.75, 14.96)	0.29	71
	(15.0, 8.0, 15)		(14.87, 7.83, 14.85)	0.25	

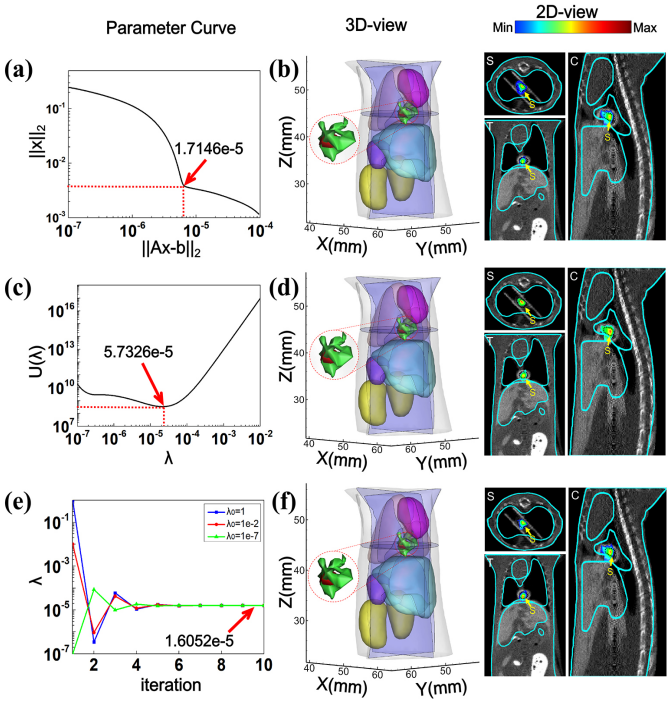

FIGURE 5 Reconstruction results of Tikhonov algorithm with regularization parameter selection strategy. (a), (c) and (e) represent the curve with L-curve algorithm, U-curve algorithm and MPD algorithm, respectively. (b), (d) and (f) represent the reconstruction results of the corresponding regularization parameters.

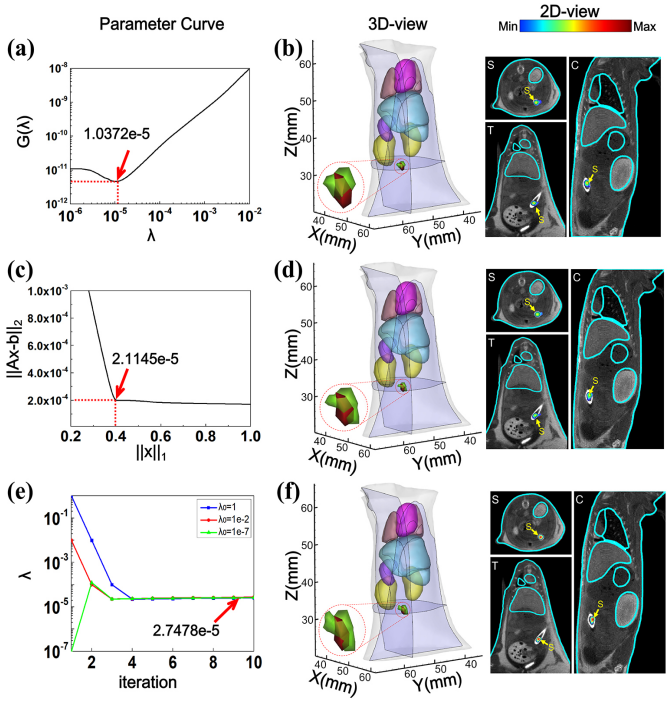

FIGURE 6 Reconstruction results of IVTCG algorithm with regularization parameter selection strategy. (a), (c) and (e) represent the curve with GCV algorithm, L_1-curve algorithm and MPD algorithm, respectively. (b), (d) and (f) represent the reconstruction results of the corresponding regularization parameters.

Dice similarity (52%) in shape recovery. In contrast, although the parameters selected by the U-curve strategy can reconstruct the real source, its positioning accuracy and reconstruction similarity are relatively poor, as shown in Table 3.

MPD strategy for L_1: Fig.6 shows the *in vivo* reconstruction results of IVTCG algorithm with regularization parameter selection strategy. From CT imgae, the center of the implanted source was located as $(56.04, 56.54, 34.36mm)$ as the red region shown in 3D view. The preset parameter range of GCV curve and L_1-curve methods are $\left(1e^{-6}, 1e^{-2}\right)$. From the log-log plots of the 50 regularization parameters in Fig. 6(a) and (c), we have marked the optimal regularization parameter points at $1.0372e^{-5}$ and $2.1145e^{-5}$, respectively. And from the fifth iterations, the proposed MPD strategy can obtain a relatively stable point($\lambda = 2.7478e^{-5}$), as Fig. 6(e) shows. From these resultes, we can find that three determined regularization parameters are at the same order of magnitude, which result in the similar energy distribution in 3D view and 2D cross section view. But in Fig.6(b), the source shape reconstructed by GCV strategy does not cover the lower half of the real source, resulting in a smallest Dice similarity (41%) in Table 3. In contrast, the reconstruction results under the L_1-curve and MPD strategy are closer to the real source, as shown in Fig. 6(d) and (f). The quantitative indicators in Table 3 further indicate that

TABLE 3 Quantitative results of single-source reconstruction experiment.

Group	Method	λ	Reconstruction Center(mm)	LE(mm)	Dice(%)
Tikhonov	L-curve	$1.71e^{-5}$	(52.81, 54.12, 44.80)	0.54	52
	U-curve	$5.73e^{-5}$	(52.82, 54.13, 44.79)	0.55	49
	MPD curve	$1.61e^{-5}$	(52.81, 54.12, 44.80)	0.54	52
IVTCG	GCV curve	$1.03e^{-5}$	(56.31, 56.47, 34.83)	0.54	41
	L_1-curve	$2.11e^{-5}$	(55.91, 56.63, 34.68)	0.35	62
	MPD curve	$2.74e^{-5}$	(55.90, 56.63, 34.65)	0.33	64

the position and shape of reconstructed results under the MPD strategy are closest to the real source, with the smallest LE ($0.33mm$) and the highest Dice(64%).

5 | DISCUSSION AND CONCLUSION

In FMT research, for a large number of clinical research needs, many effective regularized reconstruction algorithm have been proposed to alleviate the ill-posedness of source reconstruction problem. However, regularization parameters directly affect the accuracy and availability of reconstruction algorithm for different FMT application scenarios. Therefore, for most widely used L_1-norm and L_2-norm based regularization algorithms, a integrative and adaptive MPD strategy based on Bayesian theory was proposed to solve the regularization parameter selection problem by the maximum posterior estimation of the residual term and regularization term distribution. The strategy can automatically determine a stable regularization parameter and ensure the accuracy of reconstruction results.

Theoretically, MPD strategy has two distinctive innovations: (1) Based on Bayesian theory, by introducing the maximum a posteriorestimation, the strategy obtained the variance of distribution and updated the regularization parameters. Therefore, the proposed MPD strategy is an integrated solution and suitable for all reconstruction algorithms based on L_2 (Gaussian distribution) and L_1 (Laplace distribution) regularized terms. (2) Compared with some mainstream regularization parameter selection strategy (L-curve, U-curve, L_1-curve and GCV curve), MPD strategy does not need to specify a range of regularization parameters in advance. A stable regularization parameter and effective solutions can be get through several iterations by any initial value. Therefore, no pre-experiment and prior information is required to determine the selection range of regularization parameters. And the computational complexity of MPD strategy was greatly reduced and the operation efficiency is improved significantly.

In experiment part, the effectiveness and robustness of the MPD strategy were verified by a series of numerical simulations and *in vivo* experiments. Different from some researches about algorithm comparison, the major concern of our research is whether the parameters determined by MPD are consistent with existing proven and efficient methods, rather than the algorithm performance. From these comparison result, we can found that no matter what the initialization is, the MPD strategy can obtain a stable value for solving the regularization parameter determination problem based on L_2 and L_1 norm. And all regularization parameter determined by our proposed strategy and the proven strategies in existing research are in the same order of magnitude. From quantitative comparison, it demonstrate that the corresponding reconstructed results by using the MPD strategy have the best performance in source location and shape recovery with smallest LE and highest Dice. Besides that, the robustness and *in vivo* experiments also indicated that our proposed strategy has the potential to be adopted in dual-source resolution or more complex FMT pre-clinical applications. Meanwhile, we found that the dual-source reconstructed results are still unsatisfactory due to the algorithm performance limitations of Tikhonov, as shown in Fig.4 (b). Therefore, more efficient reconstruction algorithms are needed to further verify the effectiveness of MPD strategy.

Although the MPD strategy has achieved good results in parameter selection, there are two major limitations need to be further address. This work only focuses on the automatic selection of single regularization parameter. However, for some more efficient reconstruction algorithms, such as manifold learning method and hyper-regularization method[42], more parameters may be involved to be determine. Therefore, it is necessary to further study the multiple parameters determination problem by modifying the MPD strategy. Besides that, only the single source detection based on pseudotumor mouse model was conducted to verified the practicability of the MPD strategy. Some other biological applications in FMT or some other optical molucular tomography will be conducted to further illustrate the clinical significance of our study[9].

In conclusion, in order to solve the regularization parameter selection problem, an integrated and adaptive MPD strategy

was proposed by the maximum posterior estimation of distribution of the residual term and the regularization term. Compared with existed methods, MPD strategy does not need to initialize the parameter range and can converge to a stable point for most widely used L_1 and L_2-norm based regularization algorithms. Both numerical simulation and *in vivo* experiments show that MPD strategy are helpful to achieve high-precision FMT reconstruction. We believe that the proposed parameter selection strategy will help expand application range of regularization algorithms and further facilitate the preclinical and clinical FMT application.

ACKNOWLEDGMENTS

The authors would like to thank the anonymous reviewers for their useful suggestions.

FINANCIAL DISCLOSURE

This research is supported by the National Natural Science Foundation of China, Grant/Award Numbers:(61971350, 11871321, 61901374, 61906154, 82071914, 12271434, 62271394, 62201459).

CONFLICT OF INTEREST

The authors declare that they have no known competing financial interests or personal relationships that could have appeared to influence the work reported in this paper.

References

[1] Angelique Ale, Vladimir Ermolayev, Eva Herzog, Christian Cohrs, Martin Hrabé De Angelis, Vasilis Ntziachristos, *Nature methods* **2012**, *9* (6), 615–620.

[2] Nikolaos Deliolanis, Tobias Lasser, Damon Hyde, Antoine Soubret, Jorge Ripoll, Vasilis Ntziachristos, *Optics letters* **2007**, *32* (4), 382–384.

[3] Hanfan Wang, Chang Bian, Lingxin Kong, Yu An, Yang Du, Jie Tian, *IEEE Transactions on Medical Imaging* **2021**, *40* (5), 1484–1498.

[4] Hui Meng, Yuan Gao, Xin Yang, Kun Wang, Jie Tian, *IEEE transactions on medical imaging* **2020**, *39* (10), 3019–3028.

[5] Wenhui Huang, Kun Wang, Yu An, Hui Meng, Yuan Gao, Zhiyuan Xiong, Hao Yan, Qian Wang, Xuekang Cai, Xin Yang, et al., *European journal of nuclear medicine and molecular imaging* **2020**, *47* (5), 1027–1038.

[6] Peng Zhang, Chenbin Ma, Fan Song, Guangda Fan, Yangyang Sun, Youdan Feng, Xibo Ma, Fei Liu, Guanglei Zhang, *Physics in Medicine & Biology* **2022**, *67* (10), 10TR01.

[7] Yu An, Kun Wang, Jie Tian, *Visual Computing for Industry, Biomedicine, and Art* **2018**, *1* (1), 1–11.

[8] Yanqi Zhang, Guoyan Yin, Huijuan Zhao, Wenjuan Ma, Feng Gao, Limin Zhang, in *Imaging, Manipulation, and Analysis of Biomolecules, Cells, and Tissues XVI*, SPIE, **2018**, pp. 231–237.

[9] Hongbo Guo, Xiaowei He, Muhan Liu, Zeyu Zhang, Zhenhua Hu, Jie Tian, *IEEE transactions on medical imaging* **2017**, *36* (6), 1337–1346.

[10] Yu An, Jie Liu, Guanglei Zhang, Jinzuo Ye, Yang Du, Yamin Mao, Chongwei Chi, Jie Tian, *IEEE Transactions on biomedical engineering* **2015**, *62* (7), 1818–1826.

[11] Pouyan Mohajerani, Vasilis Ntziachristos, *IEEE Transactions on medical imaging* **2015**, *35* (2), 381–390.

[12] Heng Zhang, Xiaowei He, Jingjing Yu, Xuelei He, Hongbo Guo, Yuqing Hou, *Biomedical Optics Express* **2021**, *12* (12), 7807–7825.

[13] Xu Cao, Bin Zhang, Xin Wang, Fei Liu, Ke Liu, Jianwen Luo, Jing Bai, *Medical & biological engineering & computing* **2013**, *51* (8), 849–858.

[14] Hungjian Yi, Duofang Chen, Wei Li, Shouping Zhu, Xiaorui Wang, Jimin Liang, Jie Tian, *Journal of Biomedical Optics* **2013**, *18* (5), 056013.

[15] Lu Zhou, Birsen Yazici, Vasilis Ntziachristos, in *Small Animal Whole-Body Optical Imaging Based on Genetically Engineered Probes*, SPIE, **2008**, pp. 130–140.

[16] Scott C Davis, Hamid Dehghani, Jia Wang, Shudong Jiang, Brian W Pogue, Keith D Paulsen, *Optics express* **2007**, *15* (7), 4066–4082.

[17] Emmanuel J Candes, Justin K Romberg, Terence Tao, *Communications on Pure and Applied Mathematics: A Journal Issued by the Courant Institute of Mathematical Sciences* **2006**, *59* (8), 1207–1223.

[18] Junwei Shi, Fei Liu, Huangsheng Pu, Simin Zuo, Jianwen Luo, Jing Bai, *Biomedical optics express* **2014**, *5* (11), 4039–4052.

[19] Jinzuo Ye, Chongwei Chi, Zhenwen Xue, Ping Wu, Yu An, Han Xu, Shuang Zhang, Jie Tian, *Biomedical optics express* **2014**, *5* (2), 387–406.

[20] Xiaowei He, Jimin Liang, Xiaorui Wang, Jingjing Yu, Xiaochao Qu, Xiaodong Wang, Yanbin Hou, Duofang Chen, Fang Liu, Jie Tian, *Optics Express* **2010**, *18* (24), 24825–24841.

[21] Jean-Charles Baritaux, Kai Hassler, Michael Unser, *IEEE transactions on medical imaging* **2010**, *29* (4), 1075–1087.

[22] Hongbo Guo, Zhenhua Hu, Xiaowei He, Xiaojun Zhang, Muhan Liu, Zeyu Zhang, Xiaojing Shi, Sheng Zheng, Jie Tian, *Optics Express* **2017**, *25* (23), 28068–28085.

[23] Xuelei He, Jingjing Yu, Xiaodong Wang, Huangjian Yi, Yanrong Chen, Xiaolei Song, Xiaowei He, *IEEE Transactions on Biomedical Engineering* **2018**, *66* (5), 1468–1476.

[24] Per Christian Hansen, *SIAM review* **1992**, *34* (4), 561–580.

[25] Dorota Krawczyk-StanDo, Marek Rudnicki, *International Journal of Applied Mathematics and Computer Science* **2007**, *17* (2), 157.

[26] Dorota Krawczyk-Stańdo, Marek Rudnicki in *Intelligent Computer Techniques in Applied Electromagnetics*, Springer, **2008**, pp. 73–82.

[27] J Kusche, R Klees, *Journal of Geodesy* **2002**, *76* (6), 359–368.

[28] T Paul, PW Chi, Phillip M Wu, MK Wu, *Scientific reports* **2021**, *11* (1), 1–9.

[29] Maomao Chen, Han Su, Yuan Zhou, Chuangjian Cai, Dong Zhang, Jianwen Luo, *Biomedical Optics Express* **2016**, *7* (12), 5021–5041.

[30] J Nasehi Tehrani, Alistair McEwan, Craig Jin, A Van Schaik, *Applied Mathematical Modelling* **2012**, *36* (3), 1095–1105.

[31] Junwei Shi, Daiki Hara, Wensi Tao, Nesrin Dogan, Alan Pollack, John Chetley Ford, *IEEE access* **2020**, *8*, 211576–211584.

[32] Gene H Golub, Michael Heath, Grace Wahba, *Technometrics* **1979**, *21* (2), 215–223.

[33] Mahdi Roozbeh, Mohammad Arashi, Nor Aishah Hamzah, *Iranian Journal of Science and Technology, Transactions A: Science* **2020**, *44* (2), 473–485.

[34] HR Busby, DM Trujillo, *Computers & structures* **1997**, *63* (2), 243–248.

[35] Toby Sanders, Rodrigo B Platte, Robert D Skeel, *Applied Numerical Mathematics* **2020**, *152*, 29–48.

[36] Kui Ren, Gassan S Abdoulaev, Guillaume Bal, Andreas H Hielscher, *Optics letters* **2004**, *29* (6), 578–580.

[37] Alexander D Klose, Vasilis Ntziachristos, Andreas H Hielscher, *Journal of Computational Physics* **2005**, *202* (1), 323–345.

[38] Lin Yin, Kun Wang, Tong Tong, Qian Wang, Yu An, Xin Yang, Jie Tian, *IEEE Transactions on Biomedical Engineering* **2021**, *68* (11), 3388–3398.

[39] Guanglei Zhang, Fei Liu, Jie Liu, Jianwen Luo, Yaoqin Xie, Jing Bai, Lei Xing, *IEEE transactions on medical imaging* **2016**, *36* (1), 225–235.

[40] Curtis R Vogel, *Computational methods for inverse problems*, SIAM, **2002**.

[41] Xuelei He, Xiaodong Wang, Huangjian Yi, Yanrong Chen, Xu Zhang, Jingjing Yu, Xiaowei He, *Journal of biomedical optics* **2017**, *22* (4), 045009.

[42] Hongbo Guo, Jingjing Yu, Xuelei He, Huangjian Yi, Yuqing Hou, Xiaowei He, *Optics Express* **2022**, *30* (2), 1422–1441.